JOURNAL OF COMPUTATIONAL PHYSICS **136,** 640–653 (1997)
ARTICLE NO. CP975791

Hybrid Finite-Difference Method for High-Resolution Modelling of Low-Frequency Electric Induction in Humans

Trevor W. Dawson, Jan De Moerloose,[1] and Maria A. Stuchly

Department of Electrical and Computer Engineering, University of Victoria, P.O. Box 3055, Victoria, British Columbia, Canada V8W 3P6
E-mail: tdawson@ece.uvic.ca

Received December 13, 1996; revised June 25, 1997

A hybrid finite-difference technique, for modelling the induction in compact isolated heterogeneous conductors by external low-frequency time-harmonic electric fields, is described. A quasi-static finite-difference time domain code is used to model the induction in a low-resolution model of the conductor. In particular, this code solves the external problem and yields the surface charge density induced on the body. Although the internal fields are also computed, the surface charge density can be interpolated onto the surface of a higher-resolution model of the conducting body. These are then used as the source terms for a scalar-potential finite-difference code capable of solving the interior problem at an enhanced resolution, yet with a similar computational load. This paper describes the theory for integrating the two techniques. It demonstrates the validity of the technique, as applied to a human body model exposed to a 60-Hz uniform electric field. Extremely good agreement is demonstrated for the low-resolution internal fields computed by the two codes. The feasibility of the interpolation procedure and associated higher-resolution internal calculations are then illustrated.

1. INTRODUCTION

For sufficiently low-frequency electric excitation of a conducting body, the total external field must essentially be normal to the conductor surface. Consequently, the resulting external field is substantially modified from the applied one, and it is necessary to incorporate the unbounded exterior domain into any solution of the problem. This requirement has significant consequences in terms of computational resources in cases where the conducting body is complex and heterogeneous and it is required to evaluate the internal induced fields at a fairly high resolution. One particular application is in the investigation of any potentially detrimental health effects of power-frequency electric and magnetic fields on humans. The problem of computing induced field and current levels within the body is made more difficult by its complicated structure, involving components of widely varying dimensions, geometric complexity, and differing electrical properties. However, detailed anatomically based models of the human body at the millimeter resolution level are now feasible, thanks to data from the Visible Human Project (http://www.nlm.nih.gov/research/visible/visible_human.html) at the U.S. National Library of Medicine. Recently measured conductivity data suitable for low frequencies are also now available [14]. The major limitation on whole-body induction modelling is then the choice of numerical technique, and the availability of sufficient computer resources.

Finite-difference methods can be used [12, 13] to solve the interior and exterior problems simultaneously, subject to the use of appropriate grids and boundary condition. The finite-difference time-domain (FDTD) [24, 17, 21] technique can also be used to solve the full problem. For example, plane-wave induction calculations in humans at 10 MHz have been reported [16, 15], but straightforward application to lower frequencies is hampered by the time-stepping stability criterion.

For frequencies at the lower end of the spectrum, there exist alternative numerical methods which take advantage of the quasi-static approximation in either the frequency or time domain. For example, the frequency-domain *impedance method* (IM) [15] has been used [16, 23, 20] for modelling magnetic induction in humans.

A second example is a recently described quasi-static FDTD method [10]. This technique is applicable to structures where the materials can be considered as either purely dielectric (nonconducting) or sufficiently conducting that the conduction current dominates the displacement current. It uses a time-ramped excitation involving pairs of oppositely directed plane waves with the phases chosen to give purely electric or magnetic forcing in the vicinity of the body. The simulation times are short (5 ns). Results computed by this code were shown to both self-consistent and in agreement with previously published work for both electric and magnetic excitation. It was also recently shown [6] that this code gives three-figure agreement with results computed by a scalar potential fi-

[1] Now at Alcatel, Belgium.

0021-9991/97 $25.00

nite-difference (SPFD) method, for the case of magnetic excitation.

Alternatively, the source of the internal electric field may be viewed as the surface-charge density induced by the applied electric field. The solution may then be separated into two phases. The exterior problem (which depends primarily on the shape of the conductor) is solved first, typically formulated as a potential problem. One possible approach is to use Green's function-based integral equation methods [3] to solve the external problem restricted to the (bounded) body surface. The charge distribution obtained from solution of the external problem can then be incorporated into the body boundary conditions for the internal problem. Although they are not insurmountable, the two-stage integral equation method has the drawbacks of involving dense matrices, mismatched internal and external grids, and there is the possibility of numerical instability. An alternative two-stage method, combining an external finite-difference solution of Laplace's equation with an internal impedance method solution, was employed by DeFord and Gandhi [11].

The SPFD method mentioned earlier is a scalar frequency-domain code whose computational domain, like the IM, is restricted to the conducting body. In comparison with the above-mentioned methods, which all compute vector fields, an immediate advantage of a scalar method is the reduced computer storage requirements. The SPFD code has been thoroughly tested; in addition to the above-mentioned good agreement with the quasi-static FDTD code results, it also gives good agreement [7] with results based on an analytic solution [8] for low-frequency magnetic induction in an equatorially stratified conducting sphere.

For electric excitation, however, the SPFD method can only be used in the second stage of a two-phase solution process—it does not solve the exterior problem, yet it requires the induced surface charge distribution in its boundary conditions. In the present work, the quasistatic FDTD and SPFD methods are integrated into a two-stage hybrid solution scheme. As noted elsewhere [6], the numerical implementations of the two methods share some common features, particularly regarding the handling of the conductivity distribution as a set of uniform voxels. Both codes define the electric field components at the centres of the voxel edges. The SPFD code represents the potential values at the voxel vertices. Therefore, there is a one-to-one geometrical correspondence in the fields computed by the two methods for a given conductivity model and resolution, and this makes the hybrid approach feasible. The process involves running the FDTD code (effectively solving both the internal and external problems simultaneously at the lower resolution) and extracting the surface charge distribution. The usefulness of the hybrid approach arises from the possibility of interpolating the surface charge distribution onto a more realistic, higher resolution model of the conductor and subsequently using the SPFD to calculate the internal fields.

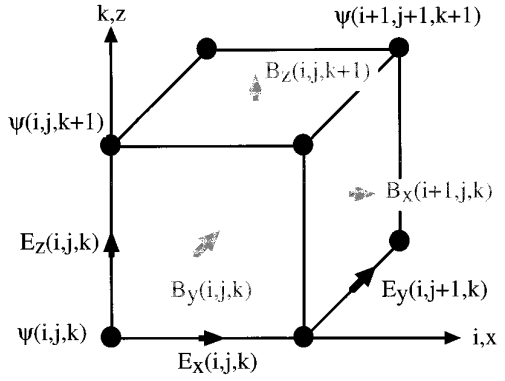

FIG. 1. Representative discrete electric and magnetic field vectors, defined on conjugate staggered grids associated with the voxel edges and faces. The figure also illustrates representative discrete samples of the conduction potential at the nodes defined by the voxel vertices.

The theory underlying the hybrid model and two-stage solution process is described in Section 2. The approach is illustrated in Section 3, using anatomically derived human body models based on cubic voxels having 7.2-mm and 3.6-mm edges. The FDTD and SPFD interior calculations are compared on the lower resolution model and found to be in excellent agreement, thereby confirming the feasibility of the hybrid approach. The surface charge interpolation and subsequent SPFD computation of the internal fields in the higher-resolution model are also demonstrated.

Although illustrated in a bioelectromagnetic context, the method is clearly applicable to low-frequency induction modelling in other complicated general heterogeneous conductors.

2. METHOD OF ANALYSIS

2.1. *Human Body Model*

A model of the human body was developed from head and torso data, based on segmentation of the magnetic

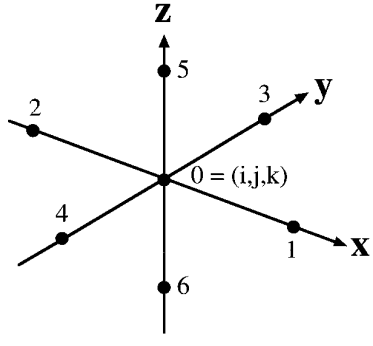

FIG. 2. Local indexing scheme at a node.

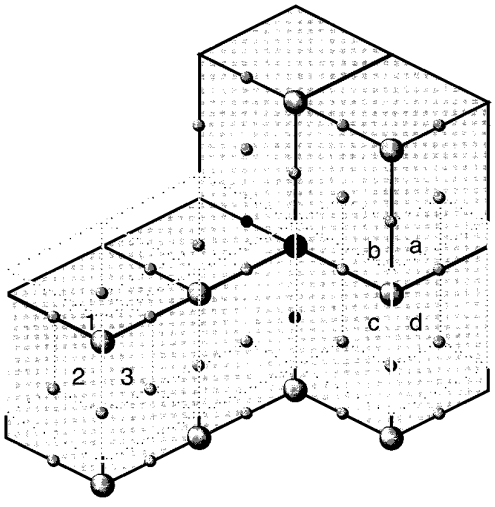

FIG. 3. Representation of a portion of surface of the voxel-based conductor. The larger spheres represent the nodes of the coarse mesh, which are also members of the high-resolution one. The small spheres represent the remaining nodes of the fine mesh. The dashed lines represent the imaginary offset voxels used for charge extraction from the FDTD low-resolution runs. The nodes shaded solid black are to be interpreted as lying inside the conductor.

resonance images (MRI), obtained from Yale Medical school [25]. The body model was completed by attaching legs and arms to the Yale model, based on representations obtained by applying segmentation algorithms developed in our laboratory to CT and MRI data from the Visible Human Project at the U.S. National Library of Medicine. The limb dimensions were scaled to match the torso, and additional manual editing was done in the planes of attachment. The height of the final body model was 1.77 m, with an estimated weight of 76 kg. The original model resolution was 3.6 mm along each Cartesian direction, with the x, y, and z axes directed from left-to-right, back-to-front, and foot-to-head, respectively. The final high-resolution body is thus represented as a set of uniform cubic voxels with 3.6-mm edges, set within an insulating air cushion in a bounding box containing $147 \times 85 \times 489$ voxels in the x-, y-, and z-directions, respectively, for a total count of 6,110,055. Of these, 1,639,146 (about 26.8%) are associated with the body interior. A $3 \times 3 \times 3$ median filtering algorithm was then applied to this model to develop a lower resolution model composed of 7.2-mm cubic voxels. The filtering process was based on the dominant local tissue type, and the output values were restricted to lie in the table of available tissues. This avoids the introduction of ''new'' tissues which would occur if an averaging technique were used, but which also results in a lower resolution model that is not simply a subsampled version of the higher resolution one. This fact imposed some difficulties in the charge interpolation algorithm, as discussed in Section 2.5. The lower resolution model has a bounding box containing $75 \times 44 \times 245$ (= 808,500) voxels, of which 204,290 comprise the body proper.

2.2. *Geometrical Conventions*

As noted earlier, both the FDTD and SPFD codes represent the conductivity by a set of parallelepiped voxels. Within each voxel, the conductivity and electric permittivity are assigned constant values. The conductivity distribution used is described in detail by Dawson *et al.* [5]. Wherever possible, recently measured [14] conductivity values were used. The body is further assumed to be nonmagnetic, so that the magnetic permeability is assigned its vacuum value of μ_0 everywhere. The interior electric permittivity does not enter the computation of the quasi-static electric field.

In both codes, the electric fields are defined on the staggered grids formed by the voxel edges, as illustrated in Fig. 1. Also associated with the rth edge is a conductance,

$$s_r \equiv \overline{\sigma}_r a_r / l_r. \tag{1}$$

Here $\overline{\sigma}_r$ denotes the average conductivity of the four voxels contacting the edge, a_r is the area of the voxel face normal

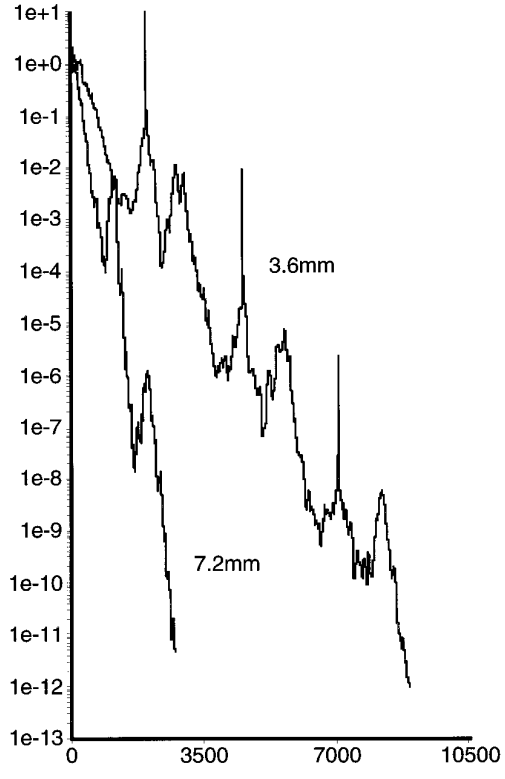

FIG. 4. Relative residual as a function of iteration number for the low- and high-resolution SPFD runs with the model located in free space.

TABLE I

Method Validation Data for the Induced Electric Field for the Body in Free Space under the Influence of a 1-kV m^{-1}, 60-Hz Vertical Electric Field

Free space	(mVm^{-1})	E_x	E_y	E_z	$\|\boldsymbol{E}\|$
Min	FDTD	−5.439868	−5.439673	−1.478571	+0.000000
	Hybrid	−5.435530	−5.439588	−1.477353	+0.000000
	Δ	−0.798056	−0.369113	−0.036375	−0.000245
Max	FDTD	+4.547296	+3.883192	+8.549955	+8.692496
	Hybrid	+4.542744	+3.879148	+8.550001	+8.692543
	Δ	+0.989263	+1.695590	+2.959168	+3.210898
Avg	FDTD	−0.000183	−0.010907	+0.567973	+0.624314
	Hybrid	−0.000015	−0.012064	+0.563913	+0.619734
	Δ	−0.000169	+0.001158	+0.004059	+0.004580
Std	FDTD	+0.188499	+0.298265	+1.124617	+1.233091
	Hybrid	+0.187913	+0.297088	+1.118736	+1.226454
	Δ	+0.013835	+0.027049	+0.062353	+0.069405
	$1 - \chi$	2.7×10^{-3}	4.12×10^{-3}	3.05×10^{-3}	3.16×10^{-3}

Note. The bottom row contains the (dimensionless) mismatch $1 - \chi$ between the internal fields computed by the FDTD method and hybrid methods, where χ is the whole-body three-dimensional correlation coefficient. The remaining rows contain the whole-body minimum and maximum field values, as well as the average and standard deviation, of the fields computed by the two methods and of the voxel-wise difference fields. Data are provided for the three components of the electric field, as well as for the magnitude. Units are as indicated in the table.

to it, and l_r is its length. Similarly, the magnetic fields are defined on the conjugate staggered mesh defined by the voxel face normals. In the SPFD code, the scalar potential values are assigned at the voxel vertices.

2.3. *Quasistatic FDTD Method*

The quasi-static finite-difference time-domain code is described and illustrated by De Moerloose *et al.* [10]. This is a standard FDTD code, modified to take advantage of the facts that the phase of the external and internal fields is known in the quasi-static case and that conduction currents dominate the displacement currents in the conducting media. Fields external to the conductor all have the same phase as the incident field, whereas interior fields are first order in the quasi-static approximation and so are proportional to the time-derivative of the

TABLE II

As for Table I, but for Current Density Induced in the Body in Free Space

Free space	(mAm^{-2})	J_x	J_y	J_z	$\|\boldsymbol{J}\|$
Min	FDTD	−0.900429	−0.872855	−0.147857	+0.000000
	Hybrid	−0.900018	−0.872826	−0.147735	+0.000000
	Δ	−0.000434	−0.000408	−0.000240	−0.000254
Max	FDTD	+0.753291	+0.676797	+2.405844	+2.410184
	Hybrid	+0.752951	+0.676488	+2.405818	+2.410158
	Δ	+0.000455	+0.000404	+0.000896	+0.000932
Avg	FDTD	−0.000153	−0.000108	+0.111125	+0.118499
	Hybrid	−0.000152	−0.000108	+0.111081	+0.118451
	Δ	−0.000001	+0.000000	+0.000044	+0.000048
Std	FDTD	+0.031216	+0.040140	+0.228689	+0.241244
	Hybrid	+0.031204	+0.040131	+0.228606	+0.241155
	Δ	+0.000019	+0.000017	+0.000091	+0.000098
	$1 - \chi$	1.0×10^{-7}	6.0×10^{-8}	2.0×10^{-8}	2.0×10^{-8}

TABLE III

As for Table I, but for the Body in Electrical Contact with a Ground Plane at the Soles of the Feet

Grounded	(mVm^{-1})	E_x	E_y	E_z	$\|\boldsymbol{E}\|$
Min	FDTD	−16.151130	−22.914816	−3.739307	+0.000000
	Hybrid	−16.159490	−22.928365	−3.728420	+0.000000
	Δ	−1.394010	−0.611820	−0.123447	−0.018132
Max	FDTD	+20.816423	+16.012054	+47.239874	+48.076987
	Hybrid	+20.828587	+16.019321	+47.257892	+48.095119
	Δ	+1.698839	+2.878240	+4.862440	+5.297610
Avg	FDTD	+0.004987	−0.012484	+1.567860	+1.704308
	Hybrid	+0.005311	−0.014597	+1.560411	+1.695746
	Δ	−0.000324	+0.002113	+0.007450	+0.008562
Std	FDTD	+0.613903	+0.863789	+3.909760	+4.157263
	Hybrid	+0.613274	+0.862472	+3.902201	+4.148403
	Δ	+0.024170	+0.047067	+0.107880	+0.120263
	$1-\chi$	7.8×10^{-4}	1.48×10^{-3}	5.5×10^{-4}	6.2×10^{-4}

incident field. The time-dependence of the incident field is ramped,

$$E_{\text{inc}} = \begin{cases} 0, & -\infty < t \le t_0, \\ \dfrac{1}{2}\left(t - \dfrac{\tau}{\pi}\sin\dfrac{\pi t}{\tau}\right), & t_0 < t \le \tau, \\ t - \tau/2, & t > \tau, \end{cases} \tag{2}$$

with a smooth start to avoid high-frequency contamination. After a short simulation time, all fields will attain either a linear (exterior) or constant (interior) time behavior. The amplitude of the fields can then be read directly from their rate of change (exterior) or their actual values (interior). To obtain a solution, it is therefore sufficient to register all field values on two subsequent time steps after the transient response has decayed. Absorbing boundary conditions [2] are used to truncate the numerical domain. On account of the retarded nature of any reflections and the short simulation times, these absorbing boundaries work

TABLE IV

As for Table II, but for the Body in Electrical Contact with a Ground Plane at the Soles of the Feet

Grounded	(mAm^{-2})	J_x	J_y	J_z	$\|\boldsymbol{J}\|$
Min	FDTD	−2.594279	−3.956228	−0.373931	+0.000000
	Hybrid	−2.594409	−3.956258	−0.372842	+0.000000
	Δ	−0.003502	−0.001606	−0.003512	−0.003542
Max	FDTD	+2.225884	+2.878188	+11.509839	+11.530188
	Hybrid	+2.226418	+2.878557	+11.508746	+11.529089
	Δ	+0.005873	+0.005240	+0.004795	+0.008791
Avg	FDTD	+0.000226	+0.001628	+0.289182	+0.308825
	Hybrid	+0.000227	+0.001627	+0.289060	+0.308667
	Δ	−0.000001	+0.000001	+0.000122	+0.000158
Std	FDTD	+0.087793	+0.111773	+0.681097	+0.712098
	Hybrid	+0.087763	+0.111747	+0.680899	+0.711863
	Δ	+0.000105	+0.000090	+0.000334	+0.000383
	$1-\chi$	6.5×10^{-7}	3.0×10^{-7}	1.1×10^{-7}	1.3×10^{-7}

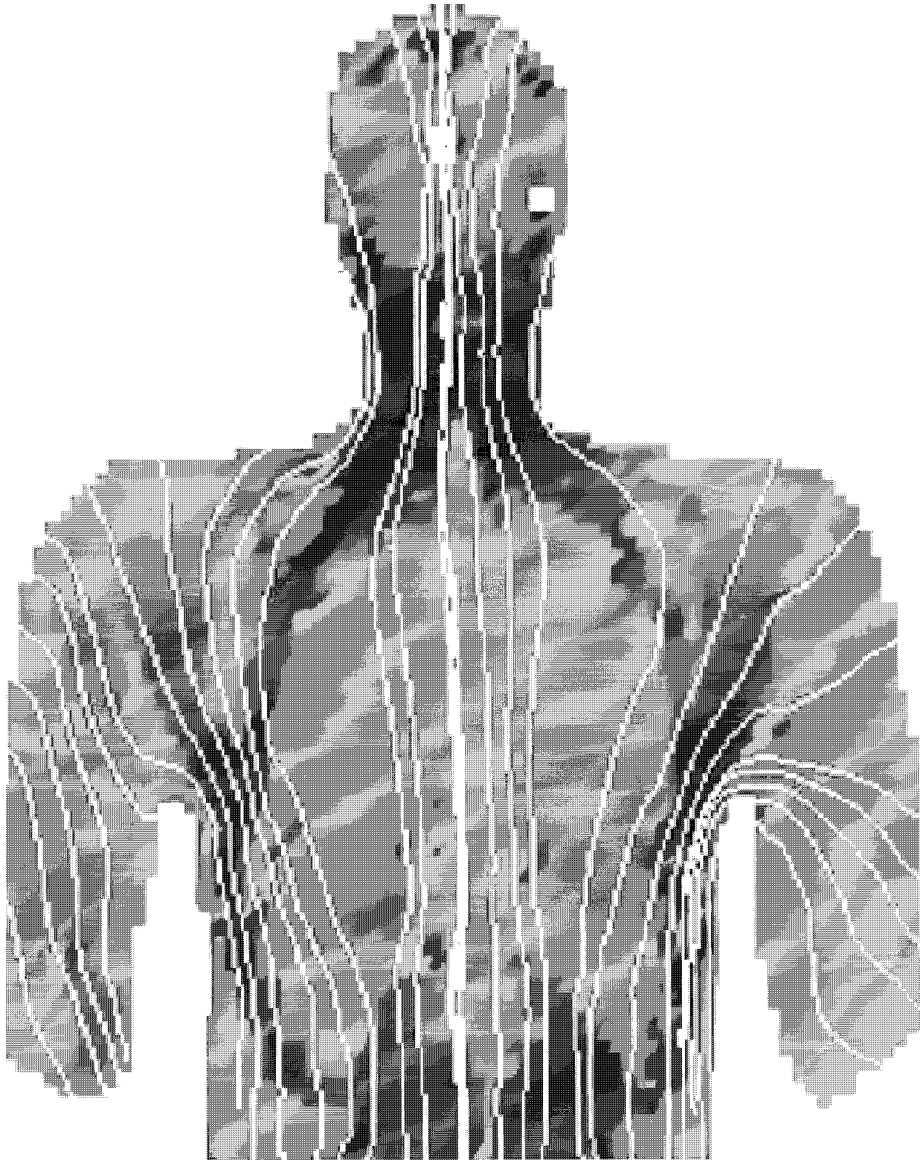

FIG. 5. Illustrations of current pseudo-streamlines in a central side-to-side cross section of the upper part of the low-resolution model situated in free space.

well for low-frequency evanescent waves, even when placed close to the conductor. Pure uniform electric or magnetic sources are generated in the vicinity of the body by an appropriate choice of the phase and polarization of pairs of oppositely traveling plane waves. Although only proven for the case of plane-wave irradiation, the quasi-static FDTD can be modified to incorporate nonuniform sources.

2.4. *SPFD Method*

The SPFD code is based on Stevenson's method [22] for quasis-static induction problems. Each of the incident, scattered, and interior electromagnetic fields can be expanded near the conductor in a power series involving the parameter $(-jk_0L)$, where k_0 and L are the wavenumber of the incident field and a characteristic dimension of the body, respectively. It is further required that the body be small compared to any internal skin depth, $L \ll \delta \equiv [\omega\mu_0\sigma(\boldsymbol{r})/2]^{-1/2}$, in order that the magnetic fields generated by the currents induced in the body are negligible (in the sense that the associated secondary currents are negligible in comparison with the primary ones). This method is a mathematical formulation that readily accommodates the concept that electric and magnetic fields are decoupled at low frequencies [18]. The method can be used up to about 100 kHz for objects of the size and conductivity values

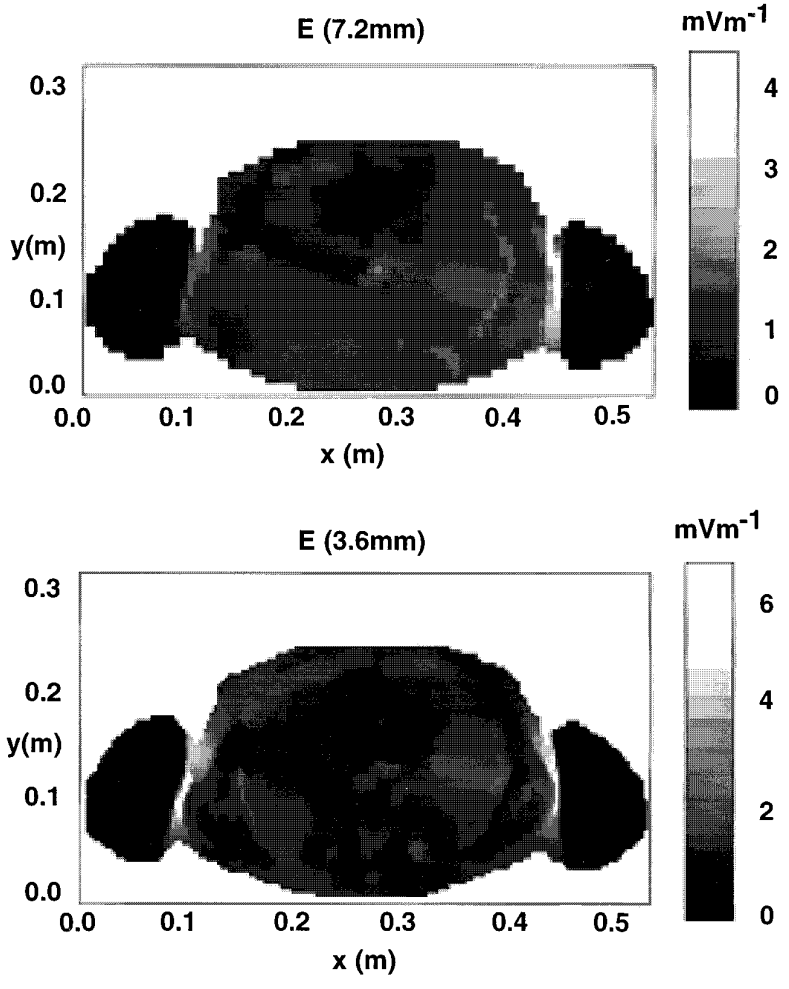

FIG. 6. Modulus of the electric field induced in a horizontal cross section through the heart for the low-resolution (top) and high-resolution (bottom) models.

of the human body. At higher frequencies, the coupling between electric and magnetic fields can no longer be neglected.

The main results are that the lowest order external magnetic field is equal to the applied field everywhere and that the external electric field can be obtained from a solution of Laplace's equation, with the body surface being one of constant potential. This gives rise to a surface charge distribution $\rho_{s0}(\boldsymbol{r})$. In the absence of any applied magnetic field, the lowest order internal electric field has the representation

$$\boldsymbol{E}_1^i(\boldsymbol{r}) = -j\omega\nabla\psi(\boldsymbol{r}). \tag{3}$$

The divergence of the associated conduction current vanishes,

$$\nabla\cdot\{\sigma(\boldsymbol{r})\boldsymbol{E}_1^i(\boldsymbol{r})\} = 0, \tag{4}$$

and the electric field must satisfy the condition

$$\sigma(\boldsymbol{r})\hat{\boldsymbol{n}}(\boldsymbol{r})\cdot\boldsymbol{E}_1^i(\boldsymbol{r}) = j\omega\rho_{s0}(\boldsymbol{r}) \tag{5}$$

at the body surface. The potential then must satisfy the differential equation

$$\nabla\cdot[\sigma(\boldsymbol{r})\nabla\psi(\boldsymbol{r})] = 0, \tag{6}$$

subject to the boundary condition

$$\sigma(\boldsymbol{r})\hat{\boldsymbol{n}}(\boldsymbol{r})\cdot\nabla\psi(\boldsymbol{r}) = -\rho_{s0}(\boldsymbol{r}). \tag{7}$$

The net result is a formulation equivalent to those of Polk and Song [19] and of Dimbylow [13].

With a local indexing scheme as depicted in Fig. 2, an application of the divergence theorem to a hypothetical

offset voxel centred on a particular node leads to the simple local finite-difference approximation

$$\left(\sum_{r=1}^{6} s_r\right)\psi_0 - \sum_{r=1}^{6} s_r\psi_r = Q_0 \tag{8}$$

to Eq. (6). The above equation needs to be modified in an obvious manner, if the central point is connected to less than six neighbouring nodes in the conductor. The term Q_0 denotes the net zeroth-order charge at any boundary node; otherwise it is zero. When an equation of the above form is written for each vertex of every conducting voxel in the distribution, the result is a heptadiagonal system of equations of the form $(N - E)y = f$. This set of equations is real, diagonally dominant, symmetric, and positive semi-definite. It is also singular, since the potential is indeterminate to within an additive constant. It can be symmetrically preconditioned to the form $(I - A)x = b$, where $A = N^{-1/2}EN^{-1/2}$, $y = N^{-1/2}x$, and $b = N^{-1/2}f$. The singularity can be removed by augmenting the system with an equation requiring that the potential have zero mean.

2.5. *Charge Interpolation*

The charge interpolation procedure is as follows. After completion of an FDTD run, a pass is made to compute the surface charge density at each current injection site, defined as a node in contact with less than six conducting edges, and at least one edge lying in external air. Each such injection site is then centred within an imaginary offset voxel, as illustrated in Fig. 3, and the associated charge evaluated from

$$Q_0 = \oiint_{\mathscr{B}} \hat{\boldsymbol{n}} \cdot (\varepsilon \boldsymbol{E})\, da, \tag{9}$$

where $\mathscr{B}$ denotes the offset voxel surface. The normal vectors are thus well defined. It may be noted that the deficiencies of staircase modelling are sidestepped in the hybrid model, since both codes employ the same geometric assumptions. The charge is subsequently converted to a surface charge density by division by the conducting voxel surface area lying within the offset one (e.g., by the total area of the three quarter-faces, labeled $1 \cdots 3$, or of the four quarter-faces labeled $a \cdots d$, at the appropriate coarse-mesh nodes in Fig. 3). Note that nodes attached to six conducting edges are to be interpreted as interior nodes, even though at the vertex of an external voxel. The resulting surface charge density is then associated with the coarse-mesh node, and the node coordinates and the associated charge density are written to a file for later use by the SPFD code.

For a coarse-grid SPFD validation run, there is a one-to-one correspondence between current injection sites in the two codes, so that the previously saved data can be used directly, being converted back to the charges required for the right-hand sides of Eq. (8).

Interpolation onto the fine mesh is slightly complicated by the fact that one is not simply a subsampled version of the other. The interpolation process therefore proceeds in three phase. Phase 1 (assignment) consists of mapping the coarse-grid charge density information onto suitable fine-mesh injection sites. As each surface charge density sample is read in, a search is made over the fine mesh model to locate the nearest conductor-based node and subsequently to locate the nearest current injection site (or equidistant sites) which is electrically connected to this target node (this is to avoid assigning charges from the torso, for example, to the arms at points of close separation). The input surface charge density is then assigned at a single site, or apportioned among the several equidistant ones. A count of multiple contributions is kept and used at the end of Phase 1 to convert to averages. In Phase 2 (broadcast) a pass is made through those injection sites assigned in Phase 1, and the surface charge density information is used to update values at the injection sites (i) which were not assigned in Phase 1 and (ii) which lie on fine-mesh faces contacting the injection sites which were assigned. For example, if the coarse mesh node (large sphere) common to quarter-faces $1 \cdots 3$ in Fig. 3 were assigned a charge density in Phase 1, then that value is common to those three subfaces, and is used to assign (partial) contributions to the associated six fine-mesh nodes (small spheres). Again, a count of partial contributions is kept and used to convert to averages at the end of Phase 2. Phase 3 (interpolation) uses a multipass search with a gradually increasing tolerance radius to interpolate existing surface charge information onto any injection sites not set during the assignment and broadcast phases.

When the above phases are complete, the surface charge density is again converted back to charge for use in the right-hand sides of Eq. (8) during a subsequent higher resolution interior SPFD run.

2.6. *Grounded Case—Mixed Conditions*

The above scheme must be modified for cases where the conductor is in electrical contact with a ground plane. In this case, the short-circuit current, entering the conductor via nodes on the ground-plane, is the quantity of interest. This is again extracted from the low-resolution FDTD computations. It is saved as current density, as opposed to charge density. The injection current density is interpolated onto the fine mesh as above. Some bookkeeping is required to restrict the surface charge interpolation to nonground plane nodes, and the current density interpola-

tion to ground-plane nodes. Integration of Eq. (4) over the body volume, followed by application of the divergence theorem and Eq. (5), leads to the expected relationship

$$I_0 = -j\omega Q_t \tag{10}$$

between the total current entering the body and the total surface charge.

3. RESULTS AND DISCUSSION

3.1. *Runs and Validation*

For the low-resolution FDTD runs, the bounding box containing the body model was surrounded by a double-voxel air layer (apart from the ground-plane wall in the grounded case), and the whole was surrounded on all sides by a 15-voxel thick absorbing boundary. Thus the calculations were performed over a $108 \times 78 \times 281$ array, for an overall domain composed of 2,367,144 voxels. Each run employed 4200 time steps of 1.2 ps for a total simulation time of 4.92 ns. Typical computation times were of the order of 18 h.

Calculations were carried out for excitation by uniform 60-Hz, 1-kV m^{-1} vertical electric source fields. The hybrid method will be illustrated with the human models placed in two situations, namely in free space, and in electrical contact with a ground plane at the soles of the feet.

In the case of the high-resolution human body model, the SPFD matrix system had 1,736,872 equations of the form (8), which was augmented by a single additional equation specifying that the conduction potential have zero mean. Solutions to this matrix system were reliably obtained using the conjugate gradient method [1] module of the parallel iterative methods package [4]. Using under 300 MB of memory on a Hewlett–Packard 9000/735 Unix workstation, the relative residuals in the iterative solutions were reduced by 12 orders of magnitude, in about 40 h. The actual time depended slightly on the body configuration. Solutions for the low-resolution model involved 229,452 potential values and were obtained in under 70 min. The convergence of the iterative solution for the body situated in free space is illustrated in Fig. 4, which plots the relative residual (in the l_2 norm) r_n/r_1 as a function of iteration number n. Similar convergence was observed for the grounded case.

To show that the hybrid procedure is viable, Table I presents a set of measures comparing the low-resolution interior electric fields computed by the FDTD code with those computed using the hybrid FDTD/SPFD scheme. This table pertains to the body located in free space, so that the SPFD inputs are purely charge-density-based. The measures are both local (whole-body maximum and minimum) and global (whole-body average and standard deviation—the latter as a measure of variation in the field), and are tabulated for the three Cartesian components, and for the magnitude, of both sets of data and of the voxel-wise difference fields. The minimum and maximum electric field values between the two methods agree to at least four significant figures. There are significant discrepancies in the voxel-wise difference fields, and the average and variation measures agree to only three significant figures. These differences are due to the presence of internal air cavities in the model. Whereas the FDTD code computes fields for all voxels in the bounding box, the SPFD code does not presently compute fields in these cavities, as they are of little bioelectromagnetic interest.

The table also shows that the highest field values ($\approx$8.5 mV m^{-1}) occur in the vertical component, as might be expected. There are, however, significant horizontal components present. This is a direct consequence of the boundary condition (5)—the current flow near the boundary has a normal component at any nonzero surface charge, and the body model surface is an approximation to one having elements with arbitrary normal orientation. Horizontal components will also be associated with the channelling of currents into tissues of higher conductivity. Finally, the table also indicates the presence of a reversed electric field (≈ -1.5 mV m^{-1}) in parts of the model. The whole-body average horizontal electric fields are almost zero, while the average vertical electric field is significantly positive ($\approx$0.57 mV m^{-1}). These features are illustrated in Fig. 5. This figure depicts projections of three-dimensional current trajectories onto a vertical, side-to-side, central cross section through the upper part of the low-resolution model situated in free space. The shading on the figure behind the streamlines is proportional to electric intensity. The asymmetry in the current flow lines, and in particular the reversed flow in the right arm, is due to an asymmetrical arrangement of the arms, particularly with respect to the minimum arm–body separation.

Also indicated in this table are the field-wise mismatches $(1 - \chi)$ between the FDTD and hybrid methods, defined in terms of the full-body three-dimensional correlation coefficients χ. These mismatches (which would be zero for perfect agreement) correspond to correlation coefficients in excess of 99.59%, for all four fields.

A better measure of the agreement between the two sets of computations is provided by the associated current density comparisons in Table II. Here the effects of internal air cavities are absent. In this case, the mismatches for all four fields correspond to whole-body correlations of better than 99.99999%. The excellent agreement is further supported by the various measures. The minimum, maximum, and variations differ in at most the fourth significant figure, and the vertical component measures are even slightly better. The measures for the magnitude of the current

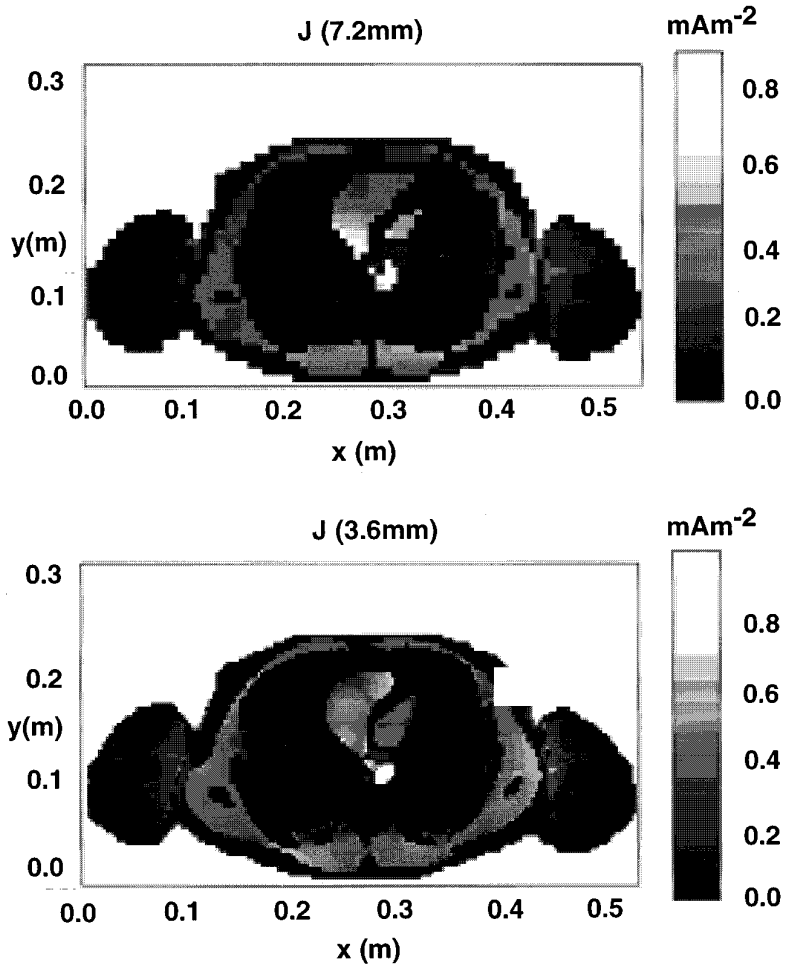

FIG. 7. Modulus of the current induced in a horizontal cross section through the heart for the low-resolution (top) and high-resolution (bottom) models.

density differ in only the fifth significant figure, apart from the variation measure.

Table III presents a similar set of measures for the electric fields induced in the grounded case, while Table IV contains the associated current density comparisons. In this case, the SPFD boundary conditions contain a mixture of charge and current. Again, the tables still indicate an excellent agreement between the two sets of interior fields.

The excellent agreement is, of course, to be expected on physical grounds—both the quasi-static FDTD code and the SPFD code implement low-frequency interpretations of Maxwell's equations. Moreover, unlike the magnetic case where the SPFD computations are decoupled from the FDTD ones and can therefore serve as an independent verification [6], the SPFD results in the hybrid method are dependent on the FDTD data. Indeed, the agreement shown in Tables I through IV is better than that obtained in the case of magnetic excitation. Nevertheless, the agreement between the hybrid and FDTD calculations provides a satisfying demonstration of the applicability of Stevenson's method to low-frequency modelling, and additionally provides an important verification of the correctness of the two distinct computer codes.

3.2. *High Resolution Examples*

To show an indication of the desirability for higher-resolution internal modelling, and to provide a introductory illustration of the associated results, Fig. 6 depicts the modulus of the electric field, taken in a horizontal cross section through the heart of the human model. The upper panel depicts the field computed in the low-resolution model, while the lower panel shows the field as computed in the high-resolution model based on the surface charge interpolation method. Figure 7 displays the current density in an analogous layout. Units and levels are indicated in the colour bars. The electric fields are fairly uniform over

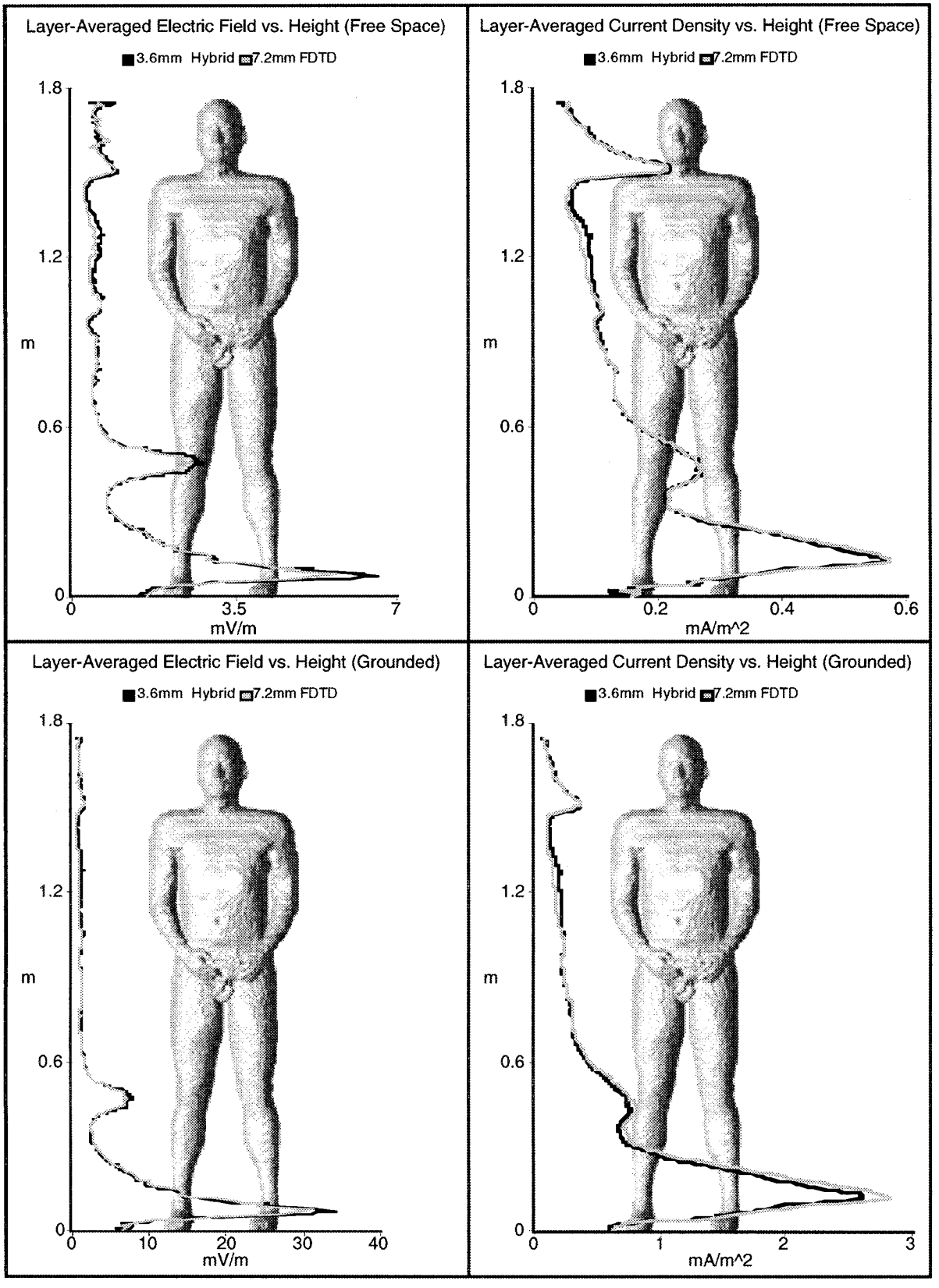

FIG. 8. Layer-averaged electric field (left column) and current density (right column) as a function of height for the body model in free space (top row) and in electrical contact with a ground plane at the soles of the feet (bottom row). The source is a 60-Hz, 1-kV m^{-1} uniform electric field directed vertically from feet to head.

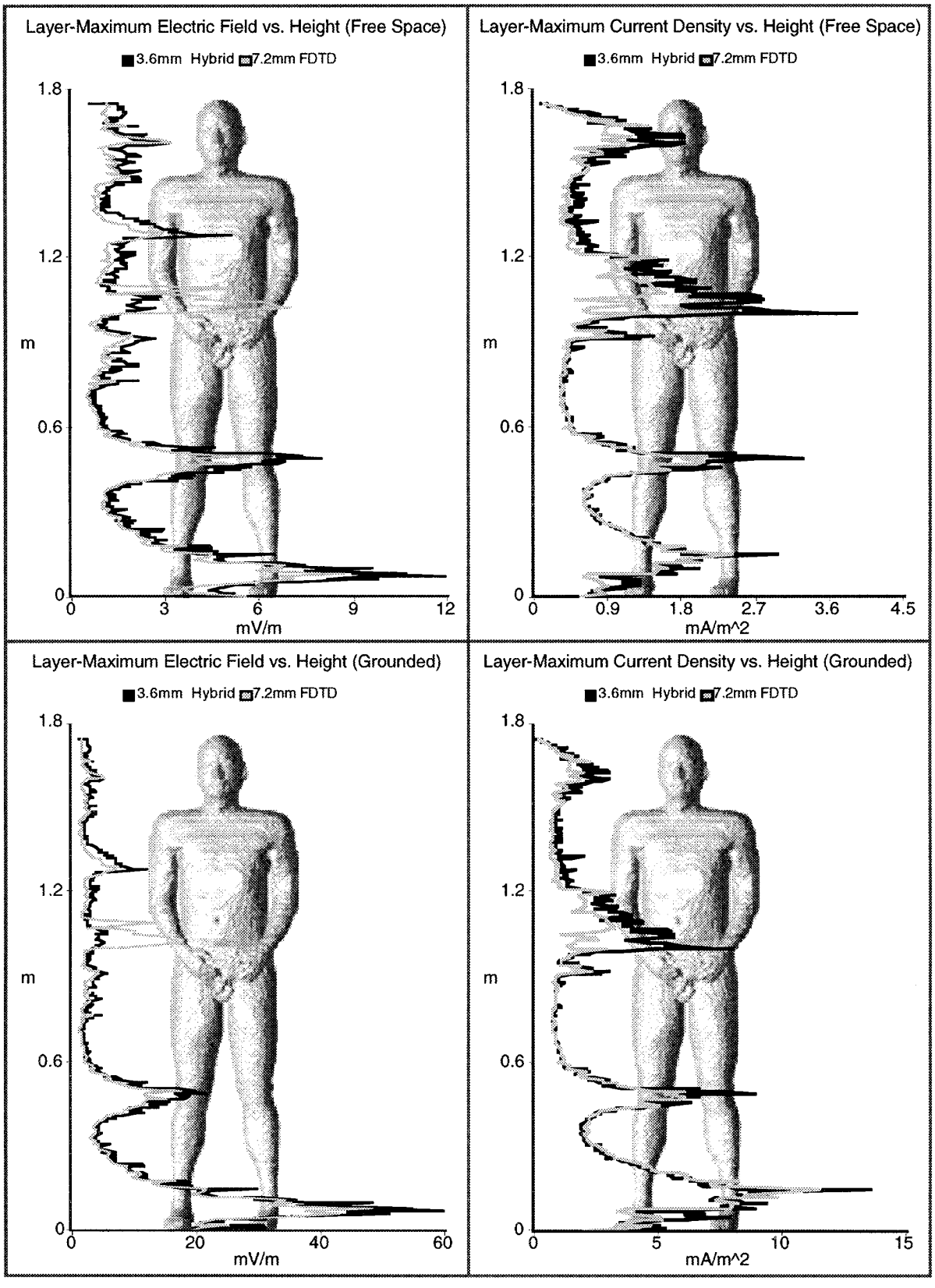

FIG. 9. Layer-maximum electric field (left column) and current density (right column) as a function of height for the body model in free space (top row) and in electrical contact with a ground plane at the soles of the feet (bottom row). The source is a 60-Hz, 1-kV m^{-1} uniform electric field directed vertically from feet to head.

much of the cross section. Details of the body interior are much more visible in the current density plots. It is quite apparent that the 7.2-mm resolution model, while adequate for representing the gross geometric properties of the model (and therefore for determining the external field and surface charge density), gives a poorer representation of the internal features.

To further illustrate the enhanced-resolution modelling, Fig. 8 presents layer-averaged data, as a function of height, for the two body configurations. The left-hand column displays the electric field intensity in millivolts per meter, while the right-hand column pertains to the current density magnitude in milliamps per square meter. The top row is for the body in free space, while the bottom row pertains to the grounded case. Each figure contains two curves, one each from the low-resolution FDTD and the high-resolution hybrid data. The identity of the curves is indicated in the legend. All curves are superimposed on a view of the high-resolution model surface. It was shown by de Moerloose *et al.* [10] that the FDTD code gave interior fields that compared favorably with other published work, when applied to an earlier body model with older conductivity values. The main focus of the present discussion is the comparison between the FDTD and hybrid calculations.

Both curves are in close agreement for the electric intensity plots. There are differences due to air cavities, visible particularly in the head (sinuses and nasopharyngeal cavities). The high-resolution computations indicate slightly higher average values, noticeable in the ankles and knees. This is consistent with the magnetic case [7], and is due to the better representation of finer scale features. The ranking is sensible, with the grounded case leading to significantly higher field levels. Similar comments apply to the current density plots, except that the high-resolution predictions are slightly lower in the ankles and knees, and more noticeably so in the grounded case. There is also a slightly higher current density in the chest.

Layer-maximum electric field and current density magnitudes are shown in a similar format in Fig. 9. There are now significant differences between results for the two model resolutions. The electric field levels are generally higher in the high-resolution model. This is as expected, since the higher resolution involves less spatial averaging in the numerical modelling. The significant differences observed in the abdomen are due to the better resolution of thin features, such as skin, fat layers, and bowel walls. Again, these results are consistent with those observed for the magnetic case [7]. Similarly, the maximum current densities (right column) are generally higher for the high-resolution model. They are quite noticeably higher in the abdomen. Discrepancies between the curves are smaller in the legs, with their generally simpler structure. The low-resolution values are generally smaller.

4. CONCLUSIONS

This work has presented a hybrid low frequency electric induction modelling method which combines a quasi-static finite-difference time-domain code with a frequency-domain scalar potential finite-difference method. The FDTD code is capable of accurately solving both the interior and exterior problems, but only at a relatively low-resolution, given limited computer resources. The SPFD code, however, is capable of solving the interior problem at higher resolution, given the surface charge distribution induced by the external electric field. This information is extracted from the FDTD results, and interpolated onto the surface of the fine-resolution model.

The validity of this hybrid method was demonstrated for the low-resolution case by the close agreement obtained between the internal fields computed solely via the FDTD method and those using the hybrid FDTD/SPFD technique.

The net result is a viable technique for modelling low-frequency electrically-induced fields in the full human body, at a resolution necessary for ascertaining the effects on smaller components such as glands.

ACKNOWLEDGMENTS

This work was supported by the NSERC/BC Hydro/TransAlta Industrial Research Chair, Ontario Hydro contract and an associated NSERC-CRD grant.

REFERENCES

1. R. Barrett, M. Berry, T. Chan, J. Demmel, J. Donato, J. Dongarra, V. Eijkhout, R. Pozo, C. Romine, and H. van der Vorst, *Templates for the Solution of Linear Systems: Building Blocks for Iterative Methods* (SIAM, Philadelphia, 1994).
2. J. P. Berenger, A perfectly matched layer for the absorption of electromagnetic waves, *J. Comput. Phys.* **114,** 185 (1994).
3. K. M. Chen, H. R. Chuang, and C. J. Lin, Quantification of interaction between ELF-LF electric fields and human bodies, *IEEE Trans. Biomed. Eng.* **BME-33**(8), 1273 (1986).
4. R. D. da Cunha and T. R. Hopkins, PIM 2.0: Parallel iterative methods package for systems of linear equations (FORTRAN 77 version), 1993. [© 1993 R. D. da Cunha, T. R. Hopkins, and Computing Laboratory, University of Kent at Canterbury, Canterbury, U.K. and Centro de Processamento de Dados, Universidade Federal do Rio Grande do Sul, Porto Alegre, Brazil].
5. T. W. Dawson, K. Caputa, and M. A. Stuchly, Influence of human model resolution on computed currents induced in organs by 60-Hz magnetic fields, *Bioelectromagn. J.* (1997), in press.
6. T. W. Dawson, J. De Moerloose, and M. A. Stuchly, Comparison of magnetically induced ELF fields in humans computed by FDTD and scalar potential FD codes, *Appl. Comput. Electromagn. Soc. J.* **11**(3), 63 (1996).
7. T. W. Dawson and M. A. Stuchly, analytic validation of a three-dimensional scalar-potential finite-difference code for low-frequency magnetic induction, *Appl. Comput. Electromagn. Soc. J.* **11**(3), 72 (1996).

8. T. W. Dawson and M. A. Stuchly, An analytic solution for verification of computer models for low-frequency magnetic induction, *Radio Sci.* **32**(2), 343 (1997).
9. T. W. Dawson, M. A. Stuchly, and K. Caputa, High-resolution organ dosimetry for human exposure to low-frequency electric fields, *IEEE Trans. Power. Eng.* (1997), in press.
10. J. De Moerloose, T. W. Dawson, and M. A. Stuchly. Application of finite difference time domain algorithm to quasi-static field analysis, *Radio Sci.* **32**(2), 329 (1997).
11. J. F. DeFord and O. P. Gandhi, An impedance method to calculate currents induced in biological bodies exposed to quasi-static electromagnetic fields, *IEEE Trans. Electromagn. Compatibility* **EMC-27**(3), 168 (1985).
12. P. J. Dimbylow, Finite difference calculations of current densities in a homogeneous model of a man exposed to extremely low frequency electric fields, *Bioelectromagnetics* **8,** 355 (1987).
13. P. J. Dimbylow, The calculation of induced currents and absorbed power in a realistic, heterogeneous model of the lower leg for applied electric fields from 60 Hz to 33 MHz, *Phys. Med. Biol.* **33**(12), 1453 (1988).
14. S. Gabriel, R. W. Lau, and C. Gabriel, The dielectric properties of biological tissues: Measurements in the frequency range 10 Hz to 20 GHz, *Phys. Med. Biol.* **41,** 2251 (1996).
15. O. P. Gandhi, Some numerical methods for dosimetry: Extremely low frequencies to microwave frequencies, *Radio Sci.* **30**(1), 161 (1995).
16. O. P. Gandhi and J.-Y. Chen, Numerical dosimetry at power-line frequencies using anatomically based models, *Biolelectromagn. Suppl.* **1,** 43 (1992).
17. K. S. Kunz and R. J. Luebbers, *Finite Difference Time Domain Method for Electromagnetics* (CRC Press, Boca Raton, FL, 1993).
18. R. G. Olsen, Power-transmission electromagnetics, *IEEE Antennas & Propag. Mag.* **36**(6), 7 (1994).
19. C. Polk and J. H. Song, Electric fields induced by low frequency magnetic fields in inhomogeneous biological structures that are surrounded by an electric insulator, *Bioelectromagnetics* **11,** 235 (1990).
20. M. A. Stuchly and S. Zhao, Magnetic field-induced currents in the human body in proximity of power lines, *IEEE Trans. Power Delivery* **11,** 102 (1996).
21. A. Taflove, *Computational Electrodynamics: The Finite-Difference Time-Domain Method* (Artech House, Norwood, MA, 1995).
22. J. Van Bladel, *Electromagnetic Fields*, rev. ed. (Hemisphere, Washington, DC 1985).
23. W. Xi, M. A. Stuchly, and O. P. Gandhi, Induced electric currents in models of man and rodents from 60 Hz magnetic fields, *IEEE Trans. Biomed. Eng.* **BME-41**(11), 1018 (1994).
24. K. S. Yee, Numerical solutions to initial boundary value problem involving Maxwell's equations in isotropic media, *IEEE Trans. Antennas Propag.* **14,** 302 (1966).
25. I. G. Zubal, C. R. Harrell, E. O. Smith, Z. Rattner, G. R. Gindi, and P. H. Hoffer, Computerized three-dimensional segmented human anatomy, *Phys. Med. Biol.* **21,** 299 (1994).